Casimir microsphere diclusters and three-body effects in fluids

Jaime Varela,[1] Alejandro W. Rodriguez,[2] Alexander P. McCauley,[1] and Steven G. Johnson[3]

[1]*Department of Physics, Massachusetts Institute of Technology, Cambridge, Massachusetts 02139, USA*

[2]*School of Engineering and Applied Sciences, Harvard University, Cambridge, Massachusetts 02139, USA*

[3]*Department of Mathematics, Massachusetts Institute of Technology, Cambridge, Massachusetts 02139, USA*

Our previous paper [Phys. Rev. Lett. **104**, 060401 (2010)] predicted that Casimir forces induced by the material-dispersion properties of certain dielectrics can give rise to stable configurations of objects. This phenomenon was illustrated via a dicluster configuration of nontouching objects consisting of two spheres immersed in a fluid and suspended against gravity above a plate. Here, we examine these predictions from the perspective of a practical experiment and consider the influence of nonadditive, three-body, and nonzero-temperature effects on the stability of the two spheres. We conclude that the presence of Brownian motion reduces the set of experimentally realizable silicon-teflon spherical diclusters to those consisting of layered microspheres, such as the hollow core (spherical shells) considered here.

I. INTRODUCTION

In this paper, we investigate the influence of nonadditive (three-body) and nonzero-temperature effects on our earlier prediction that the Casimir force (which arises from quantum electrodynamic fluctuations [1–4]) can enable dielectric objects (microspheres) with certain material dispersions to form stable nontouching configurations (diclusters) in fluids [5,6]. Such microsphere interactions are predicted to possess a variety of unusual Casimir effects, including repulsive forces [7–9], a strong interplay with material dispersion [5], and strong temperature dependences [10], and may have applications in microfluidic particle suspensions [11,12]. A typical situation considered in this paper is depicted in Fig. 1, consisting of silicon and teflon microspheres suspended in ethanol above a gold substrate. Although our earlier work considered pairs of microspheres suspended above a substrate in the additive or pairwise approximation, summing the exact two-body sphere-sphere and sphere-substrate interactions, in this paper we perform exact three-body calculations. In Sec. II, we explicitly demonstrate the breakdown of the pairwise approximation for sufficiently small spheres, in which an adjacent substrate modifies the equilibrium sphere separation, but we also identify experimentally relevant regimes in which pairwise approximations [and even a parallel-plate proximity-force approximation (PFA) [13]] are valid. In Sec. III, we also consider temperature corrections to the Casimir interactions. Although a careful choice of materials can lead to a large temperature dependence stemming from the thermal change in the photon distribution [10,14,15], we find that such thermal-photon effects are negligible ($< 2\%$) for the materials considered here. However, we show that substantial modifications to the object separations occur due to Brownian motion of the microspheres. This effect can be reduced by lowering the temperature, limited by the freezing point of ethanol ($T \approx 159$ K), or by increasing the sphere diameters. We propose experimentally accessible geometries consisting of hollow microspheres (which can be fabricated by standard methods [16]) whose dimensions are chosen to exhibit a clear stable nontouching equilibrium in the presence of Brownian

fluctuations. We believe that this work is a stepping stone to direct experimental observation of these effects.

In fluid-separated geometries, the Casimir force can be repulsive, leading to experimental wetting effects [17–19] and even recent direct measurements of the repulsive force in fluids for sphere-plate geometries [20–22]. In particular, for two dielectric or metallic materials with permittivity ε_1 and ε_3 separated by a fluid with permittivity ε_2, the Casimir force is repulsive when $\varepsilon_1 < \varepsilon_2 < \varepsilon_3$ [7]. More precisely, the permittivities depend on frequency ω, and the sign of the force is determined by the ordering of the $\varepsilon_k(i\kappa)$ values at imaginary frequencies $\omega = i\kappa$ (where ε_k is purely real and positive for any causal passive material [7]). If the ordering changes for different values of κ, then there are competing repulsive and attractive contributions to the force. At larger or smaller separations, smaller or larger values of κ, respectively, dominate the contributions to the total force, and so the force can change sign with separation. For example, if $\varepsilon_1 < \varepsilon_2 < \varepsilon_3$ for large κ and $\varepsilon_1 < \varepsilon_3 < \varepsilon_2$ for small κ, then the force may be repulsive for small separations and attractive for large separations, leading to a stable equilibrium at an intermediate nonzero separation. Alternatively, for a sphere-plate geometry in which the sphere is pulled downward by gravity, a purely repulsive Casimir force (which dominates at small separations) will also lead to a stable suspension. These basic ideas were exploited in our previous work [5] to design sphere-sphere and sphere-plate geometries exhibiting a stable nontouching configuration. The effects of material dispersion are further modified by an interplay with geometric effects (which set additional length scales beyond that of the separation), as well as by nonzero-temperature effects, which set a Matsubara length scale $2\pi kT/\hbar$ [15] that can further interact with dispersion to yield strong temperature corrections [10]. Experimentally, stable suspensions are potentially appealing in that one would be measuring static displacements rather than force between microscale objects. The stable configurations may be further modified, however, by three-body effects in sphere-sphere-plate geometries and by Brownian motion of the particles within the potential well created by the Casimir interaction, and these effects are studied in detail in the present paper.
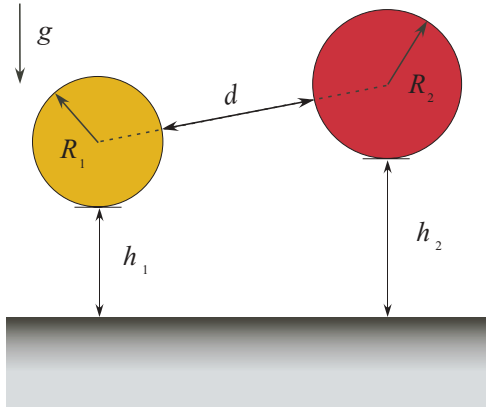
FIG. 1. (Color online) Schematic of two-sphere dicluster geometry consisting of two dielectric spheres of radii R_1 and R_2 separated by a center-center distance d from each other, and suspended by heights h_1 and h_2, respectively, above a dielectric plate.

Until the past few years, theoretical predictions of Casimir forces were limited to a small set of simple geometries (mainly planar geometries) amenable to analytical solution, but a number of computational schemes have recently been demonstrated that are capable of handling complicated (and, in principle, arbitrary) geometries and materials [23–25]. Here, since the geometries considered in this paper consist entirely of spheres and planes, we are able to adapt an existing technique [25] based on Fourier-like ("spectral") expansions that semianalytically exploits the symmetries of this problem. This technique, formulated in terms of the scattering matrices of the objects in a basis of spherical or plane waves, was developed in various forms by multiple authors [25–27], and we employ the generalization of [25]. Although this process is described in detail elsewhere [25] and is reviewed for the specific geometries of this paper in the Appendix, the basic idea of the calculation is as follows. The Casimir energy can be expressed via path integrals as an integral $\int_0^\infty \ln \det A(\kappa)d\kappa$ over imaginary frequencies κ, where A is a "T-matrix" related to the scattering matrix of the system. In particular, one needs to compute the scattering matrices relating outgoing spherical waves from each sphere (or plane waves from each plate) being reflected into outgoing spherical waves (or plane waves) from every other sphere (or plate), which can be expressed semianalytically (as infinite series) by "translation matrices" that reexpress a spherical wave (or plane wave) with one origin in terms of spherical waves (or plane waves) around the origin of the new object [25]. This formalism is exact (no uncontrolled approximations) in the limit in which an infinite number of spherical or plane waves is considered. To obtain a finite matrix A, the number of spherical waves (or spherical harmonics $Y_{\ell m}$) is truncated to a finite order ℓ. Because this expansion converges exponentially fast for spheres [25,28], we find that $\ell \leqslant 10$ suffices for $< 1\%$ errors with the geometries in this paper. (Conversion from plane waves to spherical waves is performed by a semianalytical formula [25] that involves integrals over all wave vectors, which was performed by a standard quadrature technique for semi-infinite integrals [29].) Although it is possible to differentiate $\ln \det A$ analytically to obtain a trace expression for the force [24], in this paper we use the simple expedient

of computing the energy and differentiating numerically via spline interpolation. Previously, Ref. [30] employed the same formalism to study a related geometry consisting of vacuum-separated perfect-metal spheres adjacent to a perfect-metal plate, where it was possible to employ the method of images to reduce the computational complexity dramatically. That work found a three-body phenomenon in which the presence of a metallic plate resulted on a stronger attractive interaction between the spheres, and that this effect becomes more prominent at larger separations [30], related to an earlier three-body effect predicted for cylindrical shapes [31,32]. Here, we examine dielectric spheres and plate immersed in a fluid, and therefore we cannot exploit the method of images for simplifying the calculation, which makes the calculation much more expensive because of the many oscillatory integrals that must be performed to convert between plane waves (scattering off of the plate) and spherical waves (see the Appendix). We also obtain three-body effects, in this case on the equilibrium separation distance, but find that the magnitude and sign of these effects depend strongly on the parameters of the problem.

II. THREE-BODY EFFECTS

To quantify the strength of three-body effects in the sphere-sphere-plate system of Fig. 1, we begin by computing how the zero-temperature equilibrium sphere-sphere separation d varies as a function of the sphere-plate separation h for two equal-radius spheres, as plotted in Fig. 2. To start with, we consider very small spheres, with radius $R = 25$ nm, for which the three-body effects are substantial. The separation d_h at a given h is normalized by d_∞ (d as $h \to \infty$, i.e., in the absence of the plate). Several different material combinations are shown (where X-Y-Z denotes spheres of materials X and Y and a plate of material Z): polystyrene (PS), teflon (Tef), and
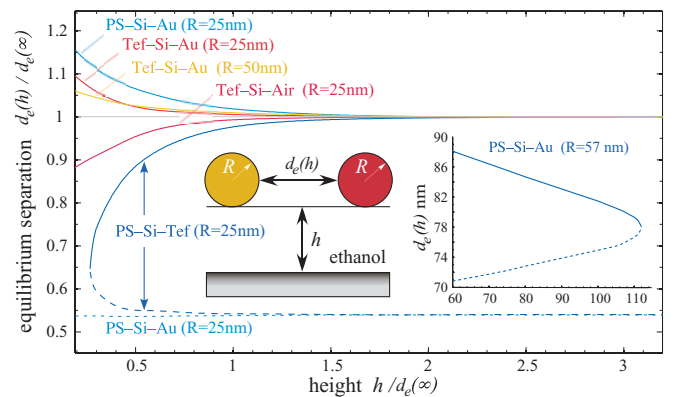

FIG. 2. (Color online) Equilibrium separation $d_e(h)/d_e(\infty)$ between two $R = 25$ nm spheres suspended in ethanol as a function of their surface-surface separation h from a plate (and normalized by the equilibrium separation for the case of two isolated spheres, i.e., $h = \infty$). d_e is plotted for various material combinations, denoted by the designation sphere-sphere-plate, e.g., a PS and silicon sphere suspended above a gold plate is denoted as PS-Si-Au. Solid (dashed) lines correspond to stable (unstable) equilibria. (In the case of a gold plate, the spheres are chosen to have $R = 50$ nm.) The inset shows d_e (in units of nm) for the case of two PS and silicon spheres ($R = 57$ nm) above a gold plate.

silicon (Si) spheres with gold (Au), teflon (Tef), and vacuum (air) plates (the latter corresponding to a fluid-gas interface). Depending on the material combinations, we find that d_h can either increase or decrease by as much as 15% as the plate is brought into proximity with the spheres from $h = \infty$ to $h \approx R$. (We expect even larger deviations when $h < R$, but small separations are challenging for this computational method [25] and our results for $h \geqslant R$ suffice here to characterize the general influence of three-body effects.)

Interestingly, depending on the material combination, the d_h can either increase or decrease as a function of h: that is, the proximity of the plate can either increase or decrease the effective repulsion. This is qualitatively similar to previous results for vacuum-separated perfect-metal spheres (plates) [30] in the following sense. Previously, the attractive interaction between a sphere and a plate was in general found to enhance the attraction between two identical spheres as the plate became closer [30]. (There are certain regimes, not present here, where the attractive interaction decreases.) Here, we observe that the sphere-plate interaction changes the sphere-sphere interaction with *the same sign* as h becomes smaller: if the sphere-plate interaction is repulsive, the sphere-sphere interaction becomes more repulsive (larger d), and vice versa for an attractive sphere-plate interaction. Since the spheres are not identical, the three-body effect is dominated by the sign of the stronger sphere-plate interaction out of the two spheres. Thus, examining the signs and magnitudes of the pairwise interactions in all cases of Fig. 2 turns out to be sufficient to predict the sign of the three-body interaction, although we have no proof that this is a general rule. (In contrast, for nonspherical objects such as cylinders, there can be competing three-body effects that make the sign more difficult to predict, even in vacuum-separated geometries where all pairwise interactions are attractive, which can even lead to a nonmonotonic effect [31,32].)

Figure 2 also exhibits the interesting phenomenon of bifurcations, in which stable equilibria (solid lines) and unstable equilibria (dashed lines) appear or disappear at some critical h for certain materials and geometries, which is discussed in more detail in Sec. II A. As the sphere radius R increases, all of these three-body effects rapidly decrease, eventually entering an additive regime in which three-body effects are negligible and in which a parallel-plate PFA approximation eventually becomes valid, as described in Sec. II B.

A. Bifurcations

In the case of PS and Si spheres suspended above either a gold or teflon plate, one can observe the emergence or disappearance of a stable (solid) and unstable (dashed) pair of equilibria as h decreases from $h = \infty$, respectively, as evidenced by the blue curves in Fig. 2 (teflon plate) and the inset (Au plate). This can be qualitatively explained by the fact that the isolated sphere-sphere interactions exhibit a natural bifurcation for sufficiently large spheres, in conjunction with the fact that the presence of the plate typically acts to either increase or decrease the sphere-sphere interaction, depending on the sign of the dominant sphere-plate interaction, as explained above.
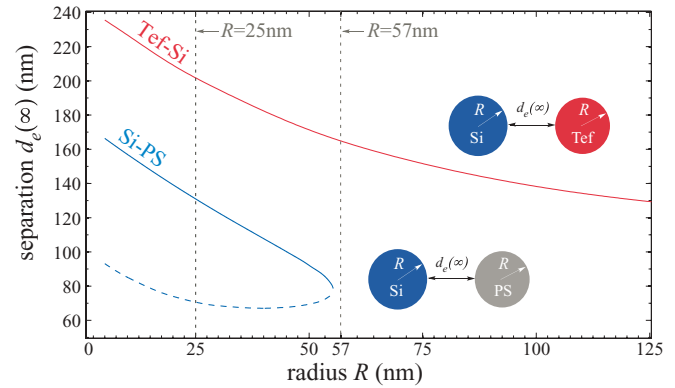

FIG. 3. Equilibrium separation $d_e(\infty)$ (units of nm) between a Si sphere and either a teflon (Tef) or polystyrene (PS) sphere immersed in ethanol as a function of their equivalent radii R. Solid (dashed) lines denote stable (unstable) equilibria.

In particular, Fig. 3 shows the isolated Si-PS and Tef-Si sphere-sphere equilibrium separation d_e as a function of the radius R of the spheres. As a consequence of its material dispersion (similar to phenomena observed in [5]), the Si-PS combination exhibits a bifurcation at $R \approx 55$ nm for the stable and unstable equilibria, such that there is no equilibrium for larger R (the interaction is purely attractive). The Tef-Si combination exhibits no such bifurcation (even if we extend the plot to $R = 300$ nm), because it has no unstable equilibrium: the interaction is purely repulsive for small separations and attractive for large separations. Therefore, if the Si-PS radius is above or below the 55 nm bifurcation, the presence of the plate can shift this bifurcation and lead to a bifurcation as a function of h as in Fig. 2, whereas no such bifurcation with h appears for Tef-Si.

In the Si-PS-Au case of a gold plate with Si-PS spheres, the sphere-plate interactions turn out to be primarily repulsive, which should push the bifurcation in Fig. 3 to the *right* (shrinking the attractive region) as h decreases. Correspondingly, if we choose a radius $R = 57$ nm just to the right of isolated-sphere bifurcation, then as h decreases, the Si-PS-Au combination should push the bifurcation past $R = 57$ nm, leading to the creation of a stable (unstable) pair for small h, and precisely this behavior is observed in the inset of Fig. 2. Conversely, for the Si-PS-Tef case of a teflon plate with Si-PS spheres, the sphere-plate interaction is primarily attractive, and the opposite behavior occurs: by choosing a radius $R = 25$ nm to the left of the isolated-sphere bifurcation, decreasing h increases the attraction and moves the bifurcation to the *left* in Fig. 3, eventually causing the disappearance of the stable (unstable) equilibrium at $R = 25$ nm. Correspondingly, for the Si-PS-Tef curve in Fig. 2, we see the disappearance of a stable (unstable) pair for sufficiently small h.

B. The additive regime

In general, three-body effects can expected to disappear in various regimes where key parameters of the interaction become small. First, for large radii, where h (the sphere-plate separation) and d (the sphere-sphere separation) become small compared to R, eventually the Casimir interaction is dominated by nearest-surface interactions, or the PFA, in which the force

can be approximated by additive surface-surface "parallel-plate" forces [13,33,34]. To damp the Brownian fluctuations as described in the next section, we actually propose to use much larger ($R > 5 \, \mu$m) spheres, and we quantify the accuracy of the PFA in this regime below. Second, as h becomes large compared to d, the effect of the plate becomes negligible and three-body effects disappear; this is apparent in Fig. 2, where $d_e \to d_e(\infty)$ when $h \gg d_e$. Third, in the limit where one of the spheres is much smaller than the other sphere, then the smaller sphere has a negligible effect on the sphere-plate interaction of the larger sphere, and at least some of the three-body effect disappears, as described below. In fact, we find that even for a situation in which one sphere is only a few times smaller than the other, the three-body effects tend to be negligible. For the sphere-radius regime considered in our previous work, we argue below that equal-height suspension of the two spheres leads to a strong asymmetry in sphere radii that tends to eliminate three-body effects.

To begin with, let us consider sphere radii on the order of 10^2 nm, as in our previous work [5]. We wish to make a bound dicluster, at some separation d, of two spheres (Si and teflon) that are suspended above a gold substrate by Casimir repulsion in balance with gravity. Furthermore, suppose that we wish to suspend both spheres at the same equilibrium height h_e, and therefore choose the radii of the two spheres to equate their h_e values. In Fig. 4, we plot h_e as a function of radius R for the isolated sphere-plate geometries ($d \to \infty$). For example, with an Si sphere of radius $R = 100$ nm, the (stable) equilibrium height is $h_e = 298.17$ nm, whereas to obtain the same h_e value for teflon, one needs a much larger teflon sphere of radius $R = 217.2$ nm, primarily because the Casimir repulsion is stronger for teflon. If, instead of a pairwise calculation, we perform an exact three-body calculation of the h_e values for these radii at the equilibrium sphere-sphere separation $d_e = 92.8$ nm, we find that the h_e values change by $< 1\%$. Conversely, if we keep h_e fixed and compute the three-body change in d_e (compared to

FIG. 4. (Color online) Center-surface L_e (solid lines) and surface-surface h_e (dotted lines) equilibrium separation (units of nm) of a teflon (red) or Si hollowed sphere (shown in the inset) suspended in ethanol above a gold plate, as a function of radius R (units of nm). The equilibria are plotted for different values of the fill fraction α, defined as the ratio of the spherical-shell thickness over the radius of the sphere. Solid (dashed) lines correspond to stable (unstable) equilibria.

$h \to \infty$), again we find that the change is $< 1\%$. As mentioned above, the small size of the Si sphere makes it unsurprising that the Si sphere does not change the equilibrium h_e of the much larger teflon sphere. Furthermore, the sensitivity of the sphere-sphere force F_d to the teflon h is equal to the sensitivity of the teflon sphere-plate force F_h to d, thanks to the equivalence $\partial F_d / \partial h = -\partial^2 U / \partial d \, \partial h = \partial F_h / \partial d$, where U is the energy. Therefore, one would also not expect the finite value of h_e for the Si sphere to modify the equilibrium d_e. Size asymmetry alone, however, does not explain why the finite h_e of the *teflon* sphere does not affect the sphere-plate interactions of the Si sphere. Even if the Si sphere were of infinitesimal radius, the Casimir-Polder energy in the Si sphere would be determined by a Green's function at the Si location [2], and if the Si sphere is at a comparable distance $d_e \sim h_e$ from both the teflon plate and the sphere, one would in general expect the response to a point-dipole source at the Si location (the Green's function) to depend nonadditively on the teflon sphere and the plate even for an infinitesimal Si sphere. However, in the present case we do not observe any nonadditive effect on the Si sphere h_e, because the factor of 3 (approximately) difference between h_e and d_e is already sufficient to eliminate three-body effects (as in Fig. 2).

Figure 4 also exhibits a bifurcation of stable (solid lines) and unstable (dashed lines) equilibria that causes the stable h equilibrium to vanish for Si at large radii. To utilize larger spheres to reduce the effects of Brownian motion in the next section, one can consider instead a geometry of hollow air-filled spherical shells with outer radius R and shell thickness αR (so that $\alpha = 1$ gives a solid sphere). Such hollow microspheres are readily fabricated with a variety of materials [16]. As Fig. 4 shows, decreasing the shell thickness α pushes the bifurcation to larger R, and also increase h_e by making the sphere more buoyant. This modification allows us to consider $R \approx 10 \, \mu$m in the next section, where the PFA should be accurate. For only 3 μm spheres and 500 nm separations in fluids, we previously found that the correction to the PFA (which scales as d/R to lowest order [35–37]) was only about 15%. For the three times larger radii and somewhat smaller separations in the next section, the corrections to the PFA are typically $< 5\%$, sufficient for our current purposes.
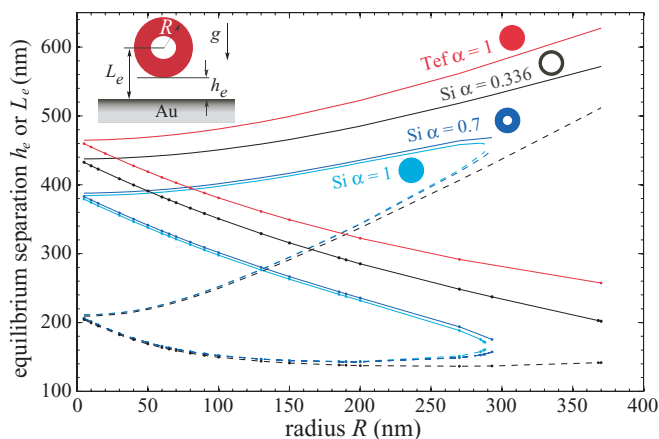
III. NONZERO TEMPERATURE AND EXPERIMENTS

In this section, we address a number of questions of consequence to an experimental realization of the teflon-silicon two-sphere dicluster of Fig. 1. In particular, we consider several ways in which a nonzero temperature can disrupt the observation of stable equilibria. A nonzero temperature will manifest itself in at least two important ways. First, there will be a change in the Casimir force between the objects due to the presence of real (nonvirtual) photons in the system. Second, the inclusion of nonzero temperature will cause the spheres to experience Brownian motion arising from the thermal agitations in the fluid [38]. We consider the influence of both of these effects on the observability of stable particle clusters and suspensions.

At zero temperature, the Casimir force F is determined by an integral $F = \int_0^\infty d\xi \, f(\xi)$ of a complicated integrand $f(\xi)$ evaluated at imaginary frequencies ξ [2]. At $T > 0$,

the integral is replaced by a finite sum over Matsubara frequencies $\omega_n = 2\pi n kT/\hbar$, arising from the poles of the coth photon distribution along the imaginary frequency axis [15,39], leading to a force F_T given by

$$F_T = \frac{2\pi kT}{\hbar} \left[\frac{f(0+)}{2} + \sum_0^\infty f\left(\frac{2\pi kT}{\hbar}n\right) \right], \qquad (1)$$

which is exactly a trapezoidal-rule approximation to the zero-temperature force with a discretization error determined by the Matsubara wavelength $\lambda_T = 2\pi c/\xi_T = \hbar/kT$ [40]. Because the integrand $f(\xi)$ is smooth and typically varies on a scale much slower than $1/\lambda_T$, where $\lambda_T = 7.6\,\mu$m at room temperature $T = 300$ K, the finite-T correction to the zero-temperature Casimir force is often negligible [3]. However, in fluids, as is the case here, larger temperature effects have been obtained [10] by dispersion-induced oscillations in $f(\xi)$, and so we must check our previous zero-temperature predictions against finite-T calculations. For the Tef-Si-substrate case considered here, we find that $T > 0$ corrections to the $T = 0$ forces are no more than 2% over the entire range of separations considered here, and hence they can be neglected.

The presence of Brownian motion proves a much more difficult experimental complication to overcome. First, Brownian motion will lead to random fluctuations in the position of the spheres, making it hard to measure their stable separations in an experiment [38]. Second, and more importantly, sufficiently large fluctuations can drive the Si sphere to "tunnel" past its unstable equilibrium position with the gold plate, leading to stiction [38] since the Si-Au interaction is purely attractive for small separations. The remainder of this section will revolve around the question of how and whether one can overcome both of these difficulties to observe suspension in experiments. In particular, we consider observation of the average separation of the spheres over a sufficiently long time, but not so long that stiction occurs, and we analyze the separation statistics and the stiction time scale. First, however, we describe how the parameters are chosen so that Brownian fluctuations are not so severe.

The sphere geometry that we consider is depicted in Fig. 5: a hollow spherical shell suspended by a surface-surface separation h above a layered substrate, consisting of a thin indium tin oxide (ITO) film of thickness H deposited on a gold substrate, where the purpose of the ITO layer is to eliminate the Si-sphere instability as explained below. The thickness of the shell is denoted as $t = \alpha R$, where α is a convenient fill-fraction parameter. We consider hollow spheres in order to increase R and thereby reduce Brownian fluctuations. In particular, both the Brownian fluctuations and the probability of stiction in the case of the silicon sphere are reduced by increasing the strength of the Casimir force, which can be achieved by increasing R since the Casimir force scales roughly with surface area, and below we consider radii from 1 to 10 μm. In this regime, as quantified in the previous section, simple PFA is sufficient to accurately compute the forces and separations. However, because the gravitational force scales as R^3, for large R the gravitational force will overcome the Casimir force and push the Si sphere past its unstable equilibrium into stiction. To reduce the gravitational force while keeping the surface area fixed, we propose using a hollow Si sphere. We find that
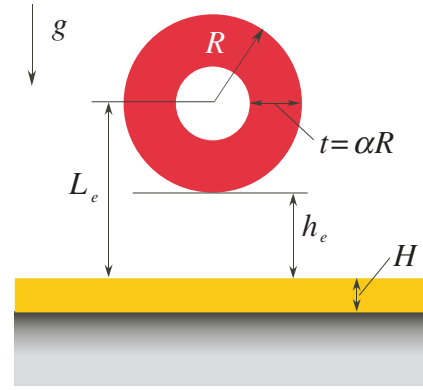

FIG. 5. (Color online) Geometry of a hollow air-filled core sphere suspended above a layered plate with layer thickness H. Explicitly shown is the thickness dimension as a function of α.

in addition to hollowing the spheres, it is also beneficial to deposit a thin ITO film on top of the gold substrate (the permittivity of ITO is modeled via an empirical Drude model with plasma frequency $\omega_p = 1.47 \times 10^{15}$ rad/s and decay rate $\gamma = 1.53 \times 10^{14}$ rad/s). The ITO layer acts to decrease the equilibria separations and therefore increase the Casimir interactions between the spheres and the substrate. However, because the Casimir force between teflon (silicon) and ITO is attractive (repulsive) at small separations, respectively, increasing H pushes the Si-substrate unstable equilibrium to smaller separations while *introducing* a teflon-substrate unstable equilibrium that gets pushed to larger separations. In what follows, we find that H from 14 to 30 nm is sufficient to obtain experimentally feasible suspensions, although here we only consider the case of $H = 15$ nm.

The effect of hollowing the spheres is shown in the top panel of Fig. 6: smaller α values push the stable (unstable) bifurcation of teflon out to larger R. Hollowing the silicon sphere is not necessary because silicon has no unstable equilibrium (in this configuration it is repulsive down to zero separation). However, as shown in the bottom panel of Fig. 6, hollowing the silicon sphere does change its h_e at a given R. For example, one can choose a Tef ($\alpha = 0.142$) and a Si ($\alpha = 0.14$) to obtain the same equilibrium surface-to-center height L_e over a wide range of sphere radii, as shown in the upper-right inset of Fig. 6. Alternatively, one can choose a hollow teflon sphere to match the equilibrium surface-surface separations h_e for equal sphere radii, as shown in the lower-right inset of Fig. 6.

A. Statistics of Brownian motion

As mentioned above, Brownian motion will disturb the spheres by causing them to move randomly about their stable equilibrium positions, and this can cause the Si sphere to move past its unstable equilibrium point, inducing it to stick to the plate. To quantify the range of motion of both spheres about their equilibria, we consider the statistical properties of their fluctuations. In particular, we consider the average plate-sphere separations $\langle h \rangle_T$ and average sphere-sphere separations $\langle d \rangle_T$ near room temperature ($T = 300$ K), determined by an
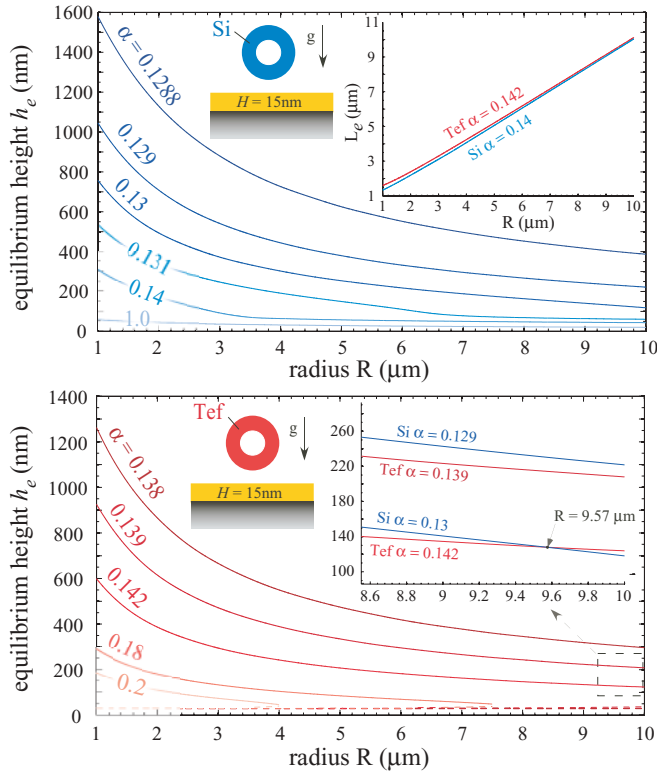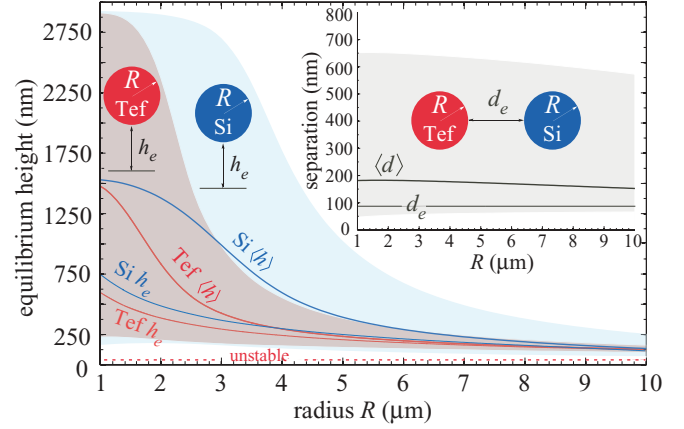
FIG. 7. (Color online) Average $\langle h \rangle$ (thick lines) and equilibrium h_e (thin lines) height (in units of nm) of a hollowed teflon (blue lines) and Si (red lines) sphere suspended above an $H = 15$ nm ITO layered gold plate, for $\alpha = 0.142$ (0.13), as a function of sphere radius R (in units of μm). Solid (dashed) lines correspond to stable (unstable) equilibria. The red (blue) shaded regions indicate positions where the teflon (Si) spheres are found with 95% probability. The inset shows $\langle d \rangle$ (thick line) and d_e (thin line) separations as a function of their radius for two equal radii teflon Si spheres. The gray shaded region indicates the separations in which the teflon and Si spheres are found with 95% probability.

FIG. 6. (Color online) Surface-surface equilibrium height h_e (units of nm) for the hollowed-sphere geometry of Fig. 5, consisting of either a Si (top) or teflon (bottom) hollowed sphere (fill fraction α) suspended in ethanol above an $H = 15$ nm ITO layered gold plate, as a function of sphere radius R (in units of μm). Solid (dashed) lines correspond to stable (unstable) equilibria. h_e is plotted for different values of α, denoted in the figure. The top inset plots the center-surface separation L_e (in units of nm) as a function of R of a hollowed teflon (red lines) and Si (blue lines) sphere suspended again above a gold plate, for $\alpha = 0.14$ (0.142). The lower inset shows h_e for both teflon and Si spheres for $R \in [8.6, 10]$ μm.

ensemble average over a Boltzmann distribution. For example, $\langle h \rangle_T$ is given by

$$\langle h \rangle_T = \frac{\int_0^\infty dz \, z \, \exp[U(z)/kT]}{\int_0^\infty dz \, \exp[U(z)/kT]}, \qquad (2)$$

where $U(z)$ is the total energy (gravity included) of the sphere-plate system at a surface-surface height z. (A similar expression yields $\langle d \rangle_T$.) In the case of teflon, the short-range attraction means that the suspension is only metastable under fluctuations; here, we only average over separations prior to stiction by restriction z to be $\geqslant$ the unstable equilibrium, and consider the stiction time scale separately below. In addition to the average equilibrium separations, we are also interested in quantifying the extent of the fluctuations of the spheres, which we do here by computing the 95% confidence interval $\{\sigma_-, \sigma_+\}$, defined as the spatial region over which the sphere is found with 95% probability around the equilibria, where $\sigma_\pm$ denotes the lower (upper) bound of that interval. These results are shown in Fig. 7 for h, with d shown in the inset, in which shaded regions indicate the confidence intervals, as a function of R, where α is chosen to yield approximately equal h_e ($\alpha = 0.142$ for teflon and $\alpha = 0.13$ for Si). (Note that

the horizontal separation $\langle d \rangle$ is a purely Casimir interaction and the difference here from $\alpha = 1$ is negligible in the PFA regime.) As predicted above, the Brownian fluctuations of the spheres vanish as $R \to \infty$ and are dramatically suppressed for $R \gtrsim 5$ μm, where one finds $\langle h \rangle \approx h_e$. In addition, we find that the teflon sphere can safely avoid the unstable equilibrium and stiction in the sense that the unstable equilibrium is far outside the confidence interval; the time scale of the stiction process is quantified below. The asymmetrical nature of the confidence interval results from the fact that the Casimir energy decreases as a function of z, and as a consequence the Brownian excursions favor the $+z$ direction. The fluctuations in $\langle d \rangle$ are substantially larger than those in $\langle h \rangle$ (nor is there any obvious reason why they should be comparable, given that the nature of the sphere-sphere equilibrium is completely different from the sphere-plate equilibrium), making the precise value of d_e potentially harder to observe.

Instead of considering the Brownian statistics as a function of R, we can instead consider the statistics as a function of α for fixed radii ≈ 10 μm (chosen to obtain nearly equal sphere-center heights L_e), as shown in Fig. 8. One key point is that there is a minimum allowed α: if α is too small, the buoyant force (assuming an air-filled hollow sphere) will eventually become positive and the sphere will float, although this limitation is removed if one could infiltrate the hollow sphere with the fluid. For the teflon sphere, there is also an upper limit to α for a given R to avoid stiction, as discussed previously.

B. Stiction and tunneling rates

As mentioned above, the stable equilibrium for the teflon sphere is actually only metastable. Because the Casimir force is attractive for small separations, given a sufficiently long
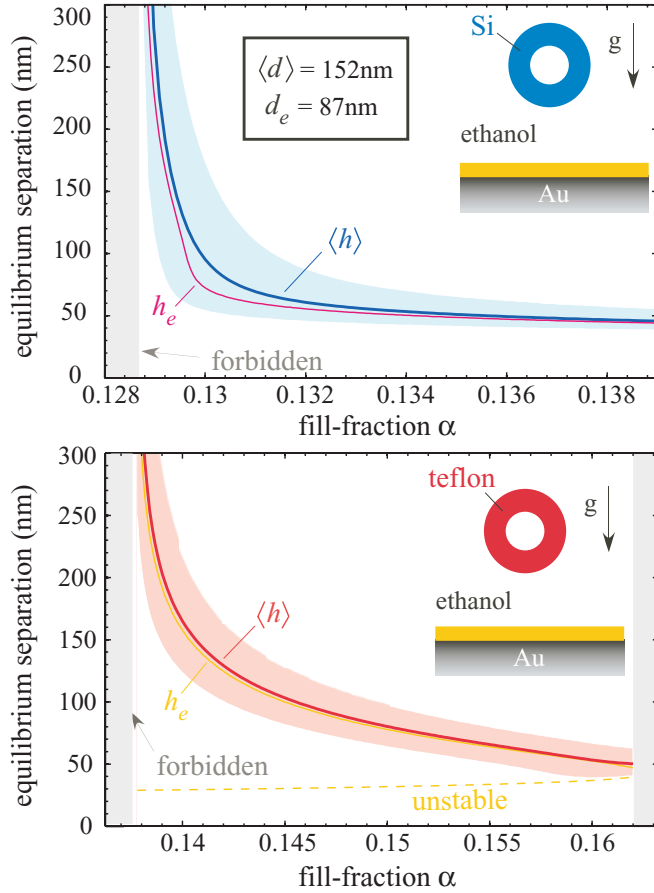
FIG. 8. (Color online) Average $\langle h \rangle$ (thick line) and equilibrium h_e (thin line) height (in units of nm) of a hollowed Si (top) and teflon (bottom) sphere of radii $R = 10$ (9.915) μm suspended in ethanol above an $H = 15$ nm ITO layered gold plate, as a function of fill fraction α (indicated in Fig. 5). Shaded regions indicate h positions where the Si (teflon) spheres are found with 95% probability. Solid (dashed) lines indicate stable (unstable) equilibria. For reference, we state the equilibrium d_e and average $\langle d \rangle$ horizontal separations between $R = 10$ (9.915) μm Si (Tef) spheres in the top figure.

observation time τ the sphere will "tunnel" (via Brownian fluctuations) past the energy barrier Δ posed by the unstable equilibrium and stick to the plate (stiction). Given the energy barrier, the temperature T, and the viscous drag on the particle, we can apply standard methods [38,41,42] to compute the time scale for stiction. This calculation, which is described in detail below, shows that for various values of the fill factor α the expected time τ to stiction (which increases exponentially with Δ / kT) can vary dramatically, but can easily be made on the order of years.

The energy barrier Δ / kT is plotted versus the teflon sphere radius R for various α in Fig. 9, and can easily be made > 10 to obtain a very long metastable lifetime. As we discussed earlier, the Δ increases with R at first because this increases the Casimir force, but it has a maximum at some R where gravity begins to dominate. Decreasing α decreases the gravitational force and therefore increases both the maximum Δ and the corresponding R. A typical energy landscape $U(z)$ is shown in the inset, exhibiting a local minimum at a height h_e and an unstable equilibrium (maximum) at h_u. Also noted in the inset
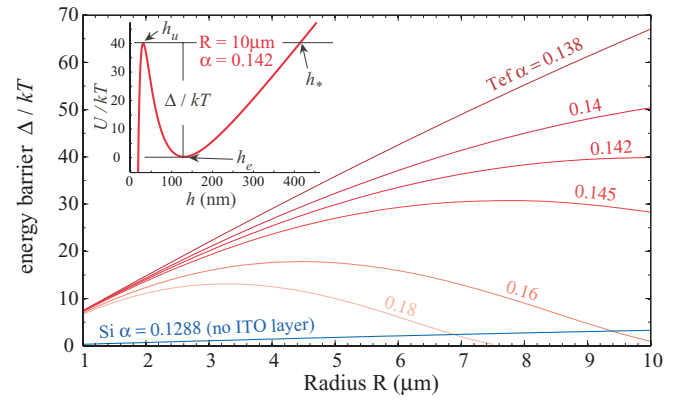

FIG. 9. (Color online) Energy barrier Δ / kT of a hollowed teflon sphere suspended in ethanol above an $H = 15$ nm ITO layered gold plate at $T = 300$ K, as a function of sphere radius R (in units of μm) and for different values of fill fraction α. The inset shows the energy landscape U/kT as a function of the surface-surface height h (units of nm) for a teflon sphere of radius $R = 10$ μm with a fill fraction of $\alpha = 0.142$.

is the "tunneling" height $h_* > h_e$ at which $U(h_*) = U(h_u)$. Figure 9 also shows the energy barrier Δ / kT of a silicon sphere ($\alpha = 0.1288 \approx \alpha_c$, $R = 10$ μm) in the absence of the ITO layer ($H = 0$) to be significantly smaller than that of teflon. Of course Δ / kT in this case could be made larger merely by choosing $\alpha \approx \alpha_c$, but we find (below) that achieving experimentally realizable lifetimes severely limits the range of realizable α, i.e., it requires that the Si thickness be known to within a few nanometers.

Because $\Delta \gg kT$, the lifetime τ of a Brownian particle trapped around a local minimum of a potential $U(z)$ can be approximated by [41]

$$\tau = e^{\Delta / kT} \left[\left(1 + \frac{\gamma}{4\omega^2} \right)^{1/2} - \frac{\gamma}{2\omega} \right]^{-1} \frac{2\pi}{\Omega} \zeta \left(\frac{\gamma S}{kT} \right), \quad (3)$$

where γ is the viscous drag coefficient (drag force = $-\gamma$ velocity), ω and Ω characterize the curvature of $U(z)$ at the energy maximum and minimum, respectively [as defined in Eq. (5)], $\zeta(\delta)$ is a transcendental function defined in Eq. (6), and S is an integral of the potential barrier defined by Eq. (4). Let m be the mass of the sphere. The drag coefficient for a sphere of radius R in a fluid with viscosity η is $\gamma = 6\pi R\eta/m$ [43], where a typical viscosity is $\eta \approx 1.17 \pm 0.06$ mPa s for ethanol [44]. The other quantities are given by

$$S = 2 \int_{h_u}^{h_c} dz \sqrt{-2mU(z)}, \quad (4)$$

$$\omega = \sqrt{\frac{U''(h_u)}{m}}, \quad \Omega = \sqrt{\frac{U''(h_e)}{m}}, \quad (5)$$

$$\zeta(\delta) = \exp \left[-\frac{2}{\pi} \int_0^{\pi/2} dz \ln \left(1 - e^{-\delta/4\cos^2 z} \right) \right]. \quad (6)$$

Combining these formulas and choosing different values of R and α to obtain different barriers Δ and landscapes $U(z)$ as in Fig. 9, the lifetime τ can be designed to take on a wide range of values. The exponential dependence on Δ means that τ rapidly transitions from very short to very long as α changes, but can easily be made large. For example, with $R = 8.5$ μm and

$\alpha < 0.15$, one obtains $\tau > 40$ days. [Conversely, for sufficiently large α one could design experiments where stiction occurs on an arbitrarily fast time scale, but in this $\Delta \sim kT$ regime the approximations of Eq. (3) are no longer valid.]

Strictly speaking, this is a conservative estimate of the time scale because the drag coefficient γ for a sphere above a plate is larger than that of an isolated sphere. As the sphere approaches the plate, the drag is dominated by the "lubrication" problem of the fluid squeezed between the sphere and the plate, and the drag increases dramatically [45].

IV. CONCLUSION

Even including thermal motion of the particles and the finite lifetime of metastable suspensions, the stable suspension and separation of particle diclusters appears to be experimentally feasible. In the experimentally relevant regimes, these effects consist primarily of pairwise sphere-sphere and sphere-plate interactions; while three-body effects become significant for smaller spheres, the increased Brownian fluctuations for small spheres make such an experiment challenging. Although the systems considered here consisted of silicon and teflon spheres above layered substrate in ethanol, many other material combinations could potentially be explored to modify these phenomena, including multimaterial sphere systems such as multilayer spheres or patterned substrates that could exhibit unusual effective dispersion phenomena. Although we considered hollow (air core) spheres, one could also use fluid-filled spheres or similar modifications to modify the effect of gravity. Alternatively, one could use nonspherical geometries such as disks, which have both a surface area and volume proportional to R^2 so that gravity does not dominate asymptotically. We have recently demonstrated computational methods capable of accurate modeling of such geometries, and find that the additional rotational degrees of freedom can lead to additional phenomena such as transitions in the stable orientation with separation [46]. In general, the possibility of both repulsion and stable equilibria in fluids (whereas the latter are not possible in vacuum [47] but do exist in critical Casimir fluids [48,49]) opens the possibility of a rich and currently little explored territory for Casimir physics, and it is likely that many effects remain to be discovered.

APPENDIX

In what follows, we write down an expression for the Casimir energy of the system in Fig. 1 in terms of the scattering and translation matrices of the individual objects (spheres and plates) of the geometry. A similar expression was derived in [30] in the case of perfect-metal vacuum-separated objects, for which an additional simplification, based on the method of images, was possible [50]. Here, we consider the more general case of fluid-separated dielectric objects.

The starting point of the Casimir-energy expression is the well-known scattering-matrix formalism, derived in [25,26], in which the Casimir energy U between an arbitrary set of objects can be written as

$$U = \frac{\hbar c}{2\pi} \int_0^\infty d\kappa \ln \det \mathbb{M}\mathbb{M}_\infty^{-1}, \tag{A1}$$

where $\mathbb{M}_\infty^{-1} = \mathrm{diag}(\mathbb{F}_1, \mathbb{F}_2, ...)$ and the matrix $\mathbb{M}$ is given by

$$\mathbb{M} = \begin{pmatrix} \mathbb{F}_1^{-1} & \mathbb{X}^{12} & \mathbb{X}^{13} & \cdots \\ \mathbb{X}^{21} & \mathbb{F}_2^{-1} & \mathbb{X}^{23} & \cdots \\ \cdots & \cdots & \cdots & \cdots \end{pmatrix}, \tag{A2}$$

where $\mathbb{F}_i(\kappa)$ is the matrix of inside or outside scattering amplitudes of the ith object, and $\mathbb{X}^{ij}$ is the translation matrix that relates the scattering matrix of the ith and jth objects, as described in [25]. Here, the plate is labeled by the index $i = 1$, whereas the left and right spheres are labeled as $i = 2$ and 3, respectively.

For computational convenience, the determinant in Eq. (A1) can be reexpressed in terms of standard operations on the block matrices composing $\mathbb{M}$, and in this case we find that

$$\det \mathbb{M}\mathbb{M}_\infty = \det(\mathcal{I} - \mathcal{N}^{(1)}) \det(\mathcal{I} - \mathcal{N}^{(2)})$$
$$\times \det[\mathcal{I} - (\mathbb{I} - \mathcal{N}^{(2)})^{-1}\mathcal{A}(\mathcal{I} - \mathcal{N}^{(1)})^{-1}\mathcal{B}],$$

where

$$\mathcal{N}^{(2)} = \mathbb{F}_3\mathbb{X}^{31}\mathbb{F}_1\mathbb{X}^{13}, \quad \mathcal{A} = F_3 X^{32} - F_3 X^{31} F_1 X^{12};$$
$$\mathcal{B} = F_2 X^{23} - F_2 X^{21} F_1 X^{13}, \quad \mathcal{N}^{(1)} = F_2 X^{21} F_1 X^{12}, \tag{A3}$$

where $(\mathcal{I} - \mathcal{N}^{(1)})$ and $(\mathcal{I} - \mathcal{N}^{(2)})$ yield the individual interaction energies of the left and right spheres with the plate, respectively. Because of the logarithm in Eq. (A1), it is possible to reexpress the energy as

$$U = \mathcal{E}_1(h_1) + \mathcal{E}_2(h_2) + \mathcal{E}_{\mathrm{int}}(h_1, h_2, d), \tag{A4}$$

where

$$\mathcal{E}_1(h_1) = \frac{\hbar c}{2\pi} \int_0^\infty d\kappa \ln \det(\mathcal{I} - \mathcal{N}^{(1)}),$$
$$\mathcal{E}_2(h_2) = \frac{\hbar c}{2\pi} \int_0^\infty d\kappa \ln \det(\mathcal{I} - \mathcal{N}^{(2)}), \tag{A5}$$

are the individual interaction energies of the left (1) and right (2) spheres above a plate, in the absence of the other sphere, and $\mathcal{E}_{\mathrm{int}}(h_1, h_2, d)$ is a three-body interaction term given by

$$\mathcal{E}_{\mathrm{int}} = \frac{\hbar c}{2\pi} \int d\kappa \ln \det[\mathcal{I} - (\mathbb{I} - \mathcal{N}^{(2)})^{-1}$$
$$\times \mathcal{A}(\mathcal{I} - \mathcal{N}^{(1)})^{-1}\mathcal{B}]. \tag{A6}$$

Finally, for completeness, we write down simplified expressions for the intermediate matrices $\mathcal{N}^{(i)}$, $\mathcal{A}$, and $\mathcal{B}$, in terms of appropriate and rapidly converging multipole and Fourier basis, as explained in [25]. The expression for $\mathcal{E}_{1,2}$ was derived in [25], and thus here we can simply quote the result for the matrices $\mathcal{N}^{(1)}$ and $\mathcal{N}^{(2)}$. In particular, [25] expresses the matrices in terms of a spherical multipole basis, indexed by the quantum numbers l, m, and P, corresponding to angular momentum, azimuthal angular momentum, and polarization [TE ($P = E$) or TM ($P = M$)]. The matrices $\mathcal{N}^{(i)}$ are given by

$$\mathcal{N}_{lmP,l'm'P'}^{(j)} = \delta_{m,m'} \mathcal{F}_{lmP,lmP}^{ee(j)} \int_0^\infty \frac{k_\perp dk_\perp}{2\pi} \frac{e^{-2h_j\sqrt{k_\perp^2 + \kappa^2}}}{2\kappa\sqrt{k_\perp^2 + \kappa^2}}$$
$$\times \sum_Q D_{lmP,k_\perp Q} r^Q D_{k_\perp Q,l'm'P'}^\dagger (2\delta_{Q,P'} - 1), \tag{A7}$$

where $\mathbf{k}_\perp$ is the Fourier momentum parallel to the plate, the $\mathcal{F}^{ee(j)}_{lmP,lmP}$ are the outside scattering amplitudes of sphere j, r^Q are the planar reflection coefficients (Fresnel reflection coefficients in the case of an isotropic plate), and $D_{lmP,k_{\perp m}}$ are conversion matrices:

$$D_{lmE,k_\perp E} = D_{lmM,k_\perp M} = \sqrt{\frac{4\pi(2l+1)(l-m)!}{l(l+1)(l+m)!}}$$
$$\times \frac{|\mathbf{k}_\perp|}{\kappa} e^{-im\phi_{\mathbf{k}_\perp}} P_l'^m\left(\sqrt{\mathbf{k}_\perp^2 + \kappa^2}/\kappa\right),$$

$$D_{lmM,\mathbf{k}_\perp E} = -D_{lmE,k_\perp M} = -im\sqrt{\frac{4\pi(2l+1)(l-m)!}{l(l+1)(l+m)!}}$$
$$\times \frac{\kappa}{\mathbf{k}_\perp} e^{-im\phi_{\mathbf{k}_\perp}} P_l^m\left(\sqrt{\mathbf{k}_\perp^2 + \kappa^2}/\kappa\right), \quad (A8)$$

given in terms of associated Legendre polynomials P_l^m and their derivatives with respect to their corresponding argument $P_l'^m$.

Upon a number of algebraic manipulations, similar expressions can be obtained for the matrices $\mathcal{A}$ and $\mathcal{B}$, not found in previous works, and in particular we find that

$$-\mathcal{A}_{lmP,l'm'P'} = \mathcal{F}^{ee}_{R,lmP,lmP}\mathcal{U}^{23}_{lmP,l'm'P'}$$
$$+(-1)^{m'-m}i^{m'-m}\mathcal{F}^{ee}_{R,lmP,lmP}\beta_{lmP,l'm'P'}, \quad (A9)$$
$$-\mathcal{B}_{lmP,l'm'P'} = \mathcal{F}^{ee}_{L,lmP,lmP}\mathcal{U}^{32}_{lmP,l'm'P'}$$

$$+ i^{m'-m}\mathcal{F}^{ee}_{L,lmP,lmP}\beta_{lmP.l'm'P'}, \quad (A10)$$

where

$$\beta_{lmP,l'm'P'} = \int_0^\infty \frac{k_\perp dk_\perp}{(2\pi)} J_{m'-m}(Sk_\perp) \frac{e^{-(h_2+h_3)\sqrt{k_\perp^2+\kappa^2}}}{2\kappa\sqrt{k_\perp^2+\kappa^2}}$$
$$\times \sum_Q D_{lmP,k_\perp Q} r^Q D^\dagger_{k_\perp Q,l'm'P'}(2\delta_{Q,P'}-1),$$
$$(A11)$$

and where the $J_m(Sk_\perp)$ is a Bessel function of the first kind evaluated at different values of $Sk_\perp$, where S is given by the projection of the sphere center-center separation onto the plate axis

$$S = \sqrt{(d+R_1+R_2)^2 - (h_1+R_1-h_2-R_2)^2}. \quad (A12)$$

From a numerical perspective, all that remains to obtain the Casimir energy in Eq. (A1) is to evaluate the various matrix entries and perform standard numerical operations, such as inversion and multiplication, which we perform using standard free software [51]. For the small matrices that we consider, most of the time is spent evaluating the various matrix elements, which can be numerically expensive due to the integration of the oscillatory Bessel functions in $\mathcal{A}$ and $\mathcal{B}$, although specialized methods for oscillatory and Bessel integrals are available that may accelerate the calculation [52,53].

[1] H. B. G. Casimir, Proc. K. Ned. Akad. Wet. **51**, 793 (1948).

[2] E. M. Lifshitz and L. P. Pitaevskiĭ, *Statistical Physics: Part 2* (Pergamon, Oxford, 1980).

[3] K. A. Milton, J. Phys. A **37**, R209 (2004).

[4] A. W. Rodriguez, F. Capasso, and S. G. Johnson, Nat. Photon. **5**, 211 (2011).

[5] A. W. Rodriguez, A. P. McCauley, D. Woolf, F. Capasso, J. D. Joannopoulos, and S. G. Johnson, Phys. Rev. Lett. **104**, 160402 (2010).

[6] A. W. Rodriguez, J. N. Munday, J. D. Joannopoulos, F. Capasso, D. A. R. Dalvit, and S. G. Johnson, Phys. Rev. Lett. **101**, 190404 (2008).

[7] I. E. Dzyaloshinski, E. M. Lifshitz, and L. P. Pitaevskǐ, Adv. Phys. **10**, 165 (1961).

[8] J. Munday, F. Capasso, and V. A. Parsegia, Nature (London) **457**, 170 (2009).

[9] O. Kenneth, I. Klich, A. Mann, and M. Revzen, Phys. Rev. Lett. **89**, 033001 (2002).

[10] A. W. Rodriguez, D. Woolf, A. P. McCauley, F. Capasso, J. D. Joannopoulos, and S. G. Johnson, Phys. Rev. Lett. **105**, 060401 (2010).

[11] S. J. Rahi and S. Zaheer, Phys. Rev. Lett. **104**, 070405 (2010).

[12] A. P. McCauley, A. W. Rodriguez, J. D. Joannopoulos, and S. G. Johnson, Phys. Rev. A **81**, 012119 (2010).

[13] B. V. Derjaguin, I. I. Abrikosova, and E. M. Lifshitz, Q. Rev. Chem. Soc. **10**, 295 (1956) [http://dx.doi.org/10.1039/QR9561000295].

[14] M. Boström and B. E. Sernelius, Phys. Rev. Lett. **84**, 4757 (2000).

[15] M. Bordag, B. Geyer, G. L. Klimchitskaya, and V. M. Mostepanenko, Phys. Rev. Lett. **85**, 503 (2000).

[16] D. Wilcox, M. Berg, T. Bernat, D. Kellerman, and J. K. Cochran, *Hollow and Solid Spheres and Microspheres: Science and Technology Associated with Their Fabrication and Application*, Vol. 372 (Society Symposium Proceedings, 1995).

[17] D. Bonn, J. Eggers, J. Indekeu, J. Meunier, and E. Rolley, Rev. Mod. Phys. **81**, 739 (2009).

[18] P.-G. de Gennes, B.-W. Francoise, and D. Quere, *Capillarity and Wetting Phenomena: Drops, Bubbles, Pearls, Waves* (Springer, 2004).

[19] J. N. Israelachvili, *Intermolecular and Surface Forces* (Elsevier, 2011).

[20] U. Mohideen and A. Roy, Phys. Rev. Lett. **81**, 4549 (1998).

[21] J. N. Munday and F. Capasso, Phys. Rev. A **75**, 060102(R) (2007).

[22] A. A. Feiler, L. Bergstrom, and M. W. Rutland, Langmuir **24**, 2274 (2008), pMID: 18278966, [http://pubs.acs.org/doi/pdf/10.1021/la7036907], [http://pubs.acs.org/doi/abs/10.1021/la7036907].

[23] A. Rodriguez, M. Ibanescu, D. Iannuzzi, J. D. Joannopoulos, and S. G. Johnson, Phys. Rev. A **76**, 032106 (2007).

[24] M. T. H. Reid, A. W. Rodriguez, J. White, and S. G. Johnson, Phys. Rev. Lett. **103**, 040401 (2009).

[25] S. J. Rahi, T. Emig, N. Graham, R. L. Jaffe, and M. Kardar, Phys. Rev. D **80**, 085021 (2009).

[26] T. Emig, N. Graham, R. L. Jaffe, and M. Kardar, Phys. Rev. Lett. **99**, 170403 (2007).

[27] O. Kenneth and I. Klich, Phys. Rev. B **78**, 014103 (2008).

[28] A. Canaguier-Durand, P. A. Maia Neto, I. Cavero-Pelaez, A. Lambrecht, and S. Reynaud, Phys. Rev. Lett. **102**, 230404 (2009).

[29] A. C. Genz and A. A. Malik, SIAM J. Numer. Anal. **20**, 580 (1983).

[30] P. Rodriguez-Lopez, S. J. Rahi, and T. Emig, Phys. Rev. A **80**, 022519 (2009).

[31] S. J. Rahi, A. W. Rodriguez, T. Emig, R. L. Jaffe, S. G. Johnson, and M. Kardar, Phys. Rev. A **77**, 030101(R) (2008).

[32] A. Rodriguez, M. Ibanescu, D. Iannuzzi, F. Capasso, J. D. Joannopoulos, and S. G. Johnson, Phys. Rev. Lett. **99**, 080401 (2007).

[33] M. Bordag, U. Mohideen, and V. M. Mostepanenko, Phys. Rep. **353**, 1 (2001).

[34] H. Gies and K. Klingmüller, Phys. Rev. Lett. **96**, 220401 (2006).

[35] P. A. Maia Neto, A. Lambrecht, and S. Reynaud, Phys. Rev. A **78**, 012115 (2008).

[36] F. D. Mazzitelli, F. C. Lombardo, and P. I. Villar, J. Phys. Condens. Matter **161**, 012015 (2009).

[37] H. Gies and K. Klingmuller, Phys. Rev. Lett. **96**, 220401 (2006).

[38] H. Risken, *The Fokker-Plank Equation: Methods of Solution and Applications* (Springer-Verlag, Heidelberg, 1996).

[39] J. Schwinger, L. L. DeRaad, and K. Milton, Ann. Phys. **115**, 1 (1978).

[40] J. P. Boyd, *Chebychev and Fourier Spectral Methods*, 2nd ed. (Dover, New York, 2001).

[41] V. I. Mel'nikov, Phys. Rep. **209**, 1 (1991), [http://www.sciencedirect.com/science/article/B6TVP-46SXR6S-DN/2/2738d111edbf3c995d7f494940a32cee].

[42] S. Chandrasekhar, Rev. Mod. Phys. **15**, 1 (1943).

[43] L. D. Landau and E. M. Lifshitz, *Fluid Mechanics* (Pergamon, Elmsford, NY, 1987).

[44] D. G. Friend and M. L. Huber, Int. J. Thermophys. **15**, 1279 (1994), [http://dx.doi.org/10.1007/BF01458836].

[45] B. Hamrock, *Fluid Film Lubrication* (McGraw-Hill, New York, 1994).

[46] M. T. H. Reid, J. White, and S. G. Johnson, e-print arXiv:1010.5539.

[47] S. J. Rahi, M. Kardar, and T. Emig, Phys. Rev. Lett. **105**, 070404 (2010).

[48] M. Tröndle, S. Kondrat, A. Gambassi, L. Harnau, and S. Dietrich, J. Chem. Phys. **133**, 074702 (2010).

[49] T. F. Mohry, A. Maciołek, and S. Dietrich, Phys. Rev. E **81**, 061117 (2010).

[50] L. S. Brown and G. J. Maclay, Phys. Rev. **184**, 1272 (1969).

[51] R. K. S. Hankin, R. News **6**, 24 (2006).

[52] S. Xiang, J. Comput. Appl. Math. **206**, 688 (2007), [http://portal.acm.org/citation.cfm?id=1265610.1265788].

[53] G. A. Evans and J. R. Webster, J. Comput. Appl. Math. **112**, 55 (1999), [http://portal.acm.org/citation.cfm?id=335447.335464].